

AFM IMAGING OF BIOLOGICAL MEMBRANES: OPTIMAL OPERATION AND DATA INTERPRETATION THROUGH UNDERSTANDING OF TRANSPORT PHENOMENA

Tai-Hsi Fan and Andrei G. Fedorov
Georgia Institute of Technology
Woodruff School of Mechanical Engineering
Atlanta, GA 30332-0405

ABSTRACT

Living cells grow and communicate with each other by exchanging ions with their environment fluid through complex physiological processes that occur in sequence and/or parallel and involve multitude of temporal and spatial scales. The events involved can be very fast and highly localized requiring spatial resolution in the order of tens of nanometers. An atomic force microscope (AFM) and AFM-based multifunctional scanning probes belong to a new class of instruments that provide a unique opportunity to study cell communication processes *in-situ* with sufficient spatial and temporal resolution. However, one of the main challenges in AFM experiments lies in data interpretation. Therefore, development of fundamentally sound, yet computationally efficient theoretical models to resolve the multiple interacting transport phenomena underlying the AFM imaging process is necessary, and such models must be general and flexible enough to simulate the complex interactions, geometry, and operating conditions of the instrument and biological membrane under actual physiological conditions. We report the electrohydrodynamic force at the surface of the AFM tip and elastic deformation of the soft biological membranes induced by the AFM probing action, which are essential for quantitative interpretation the AFM images in the aqueous environment. This study is the first theoretical demonstration, that in addition to the electrical force induced by the non-uniform electric field around the AFM tip, the feedback force at the AFM tip during imaging in an aqueous environment is also due to the strong coupling of electrohydrodynamic interactions in the solution and elastic deformation of the membrane.

INTRODUCTION

Atomic Force Microscopy (AFM) provides unique opportunities to investigate the structure, morphology, micromechanical properties, and biochemical signaling activity of cells, subcell structures, and even single molecules with high

temporal and spatial resolutions [1]. In biological applications, AFM imaging needs to be performed in the natural (aqueous) living environment of the cell in order to observe molecular level interactions and biochemical processes *in-situ* in the electrolyte solution and to avoid the interference due to the capillary adhesion forces. Despite significant advances made in experimental application of AFM in cell imaging, the data interpretation and associated theoretical models are still in their infancy. This is perhaps owing to the overwhelming complexity of the physical/chemical phenomena taking place during an AFM imaging of flexible, electrochemically active biological samples, which includes intimately coupled fluid flow (inside and outside of the cell), dynamics of the cell membrane deformation, and electrostatics of ionic interactions in the electrolyte and surface double layers. The critical importance of understanding these interactions should not be overlooked, as pointed out by Kamm in his recent review of cellular fluid mechanics [2], because of the critical role of the flow conditions on the biological functions, normal physiology and disease of living cells. In our previous work [3], the physical processes taking place during AFM imaging of soft biological membranes were investigated in detail. A particular emphasis was placed on the understanding of hydrodynamic effects in the fluid inside and outside of the cell associated with elastic deformation of the membrane in response to the AFM tapping action for the entire probing cycle. In this paper, we extend our prior work by including the electrodynamic effects on the fluid motion and surface forces to obtain an integrated electrohydrodynamic model describing the AFM tip and biomembrane interactions. The model couples the fluid flow (inside and outside of the cell membrane), equilibrium ion distribution, electrical forces, membrane surface charge, and dynamics of membrane deformation.

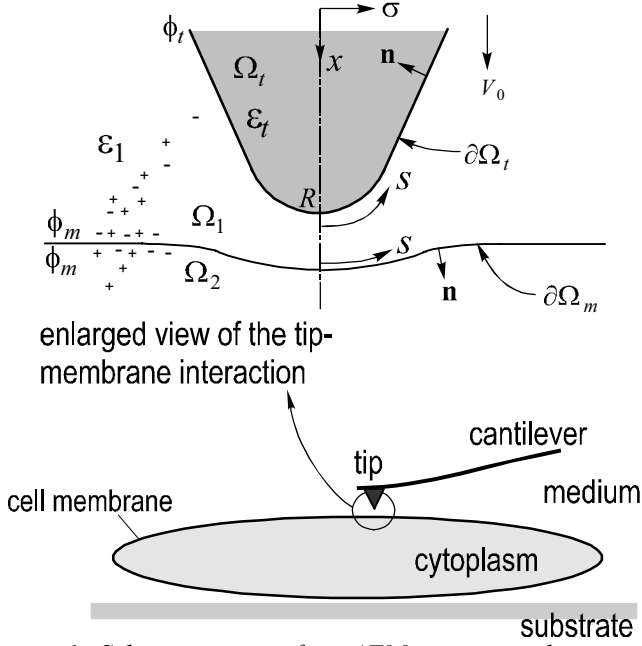


Figure 1: Schematic view of an AFM tip approaching a cell membrane and definition of the computational domain.

THEORETICAL DEVELOPMENTS

Scaling and Model Formulation

Figure 1 shows the schematic of the physical arrangement used for model development. The electrolyte is considered to be homogeneous with uniform electrical and fluid properties on both sides of the cell membrane, whose surface potential or charge density are uniform and described by a symmetric zeta potential. We also assume that the short-range van-der-Waals, hydration, and other molecular level interactions are negligible compared to the electrodynamic forces when the AFM tip penetrates into the electric double-layer of the membrane. Both the environment fluid and the fluid inside the cell are assumed incompressible Newtonian fluids with the same density and viscosity. The membrane thickness is neglected and mathematically treated as an infinitesimally thin interface. Thermal fluctuations are assumed to be negligible so that the membrane surface is perfectly smooth. We do not consider the ion transport across the cell membrane and the Lorentz electric force is the only body force involved in the probing process. The system dynamics is modeled by the electrically forced non-homogeneous Stokes equation for fluid flow, the linearized Poisson-Boltzmann equation for the electric potential distribution in the electrolyte environment, the Laplace equation for the electric potential within the dielectric AFM tip, and the Helfrich and Zhong-can's equation is used to describe the equilibrium shape of the bio-membrane. To make the results general, we render the governing equations dimensionless by using the following scales: length scale is given by the AFM tip radius R , velocity \mathbf{u} is scaled by the tip approach velocity V_0 , time is scaled by R/V_0 , the local surface tension γ is scaled by $V_0\mu$ with μ being dynamic viscosity, the membrane bending rigidity B is scaled by $V_0\mu R^2$, the membrane mean curvature H and spontaneous curvature c_0 are both scaled by $1/R$, the Gaussian curvature

K is scaled by $1/R^2$, surface force f and pressure p are scaled by $V_0\mu/R$, the electric potential ϕ is scaled by ζ ($\zeta = kT/e$) where k is Boltzmann constant, T is an absolute temperature, and e is the single electron charge. Using these scales, the dimensionless governing equations for the electric field potential and electrohydrodynamic stress are:

(i) Linearized Poisson-Boltzmann and Laplace equations [4]:

$$\nabla^2\phi = (\kappa R)^2\phi, \quad \mathbf{x} \in \Omega_1 + \Omega_2 \quad (1)$$

$$\nabla^2\phi = 0, \quad \mathbf{x} \in \Omega_t \quad (2)$$

(ii) Quasi-steady, electrically forced Stokes equation and the continuity equation with combined hydrodynamic and Maxwell electric stresses [5]:

$$\nabla \cdot (\boldsymbol{\tau}^h + \boldsymbol{\tau}^e) = -\nabla p + \nabla^2 \mathbf{u} + \alpha \phi \nabla \phi = 0, \quad \mathbf{x} \in \Omega_1 + \Omega_2 \quad (3)$$

$$\nabla \cdot \mathbf{u} = 0, \quad \mathbf{x} \in \Omega_1 + \Omega_2 \quad (4)$$

where \mathbf{x} denotes a position vector in the Cartesian coordinate system, and the volumetric charge density has been linearized about the equilibrium ion distribution. The Maxwell stress tensor and the electric field can be written in dimensionless form as

$$\boldsymbol{\tau}^e = \omega \left(\frac{\partial \phi}{\partial x_i} \frac{\partial \phi}{\partial x_j} - \frac{1}{2} \frac{\partial \phi}{\partial x_k} \frac{\partial \phi}{\partial x_k} \delta_{ij} \right), \quad \mathbf{E} = -\frac{\zeta}{R} \nabla \phi \quad (5)$$

with the term in front of the Kronecker delta δ_{ij} denoting the isotropic stress component.

(iii) Dynamic boundary condition at the membrane interface is given by the Landau's general dynamic interface model [6] combined with Helfrich membrane mechanics and Zhong-can's equilibrium shape equation [7,8], in terms of normal and shear components of the total (hydrodynamic and electric) stress tensor as described in detail in [3],

$$(\boldsymbol{\tau}_2 \cdot \mathbf{n} - \boldsymbol{\tau}_1 \cdot \mathbf{n}) \cdot \mathbf{n} = -2\gamma H + B(2H + c_0)(2H^2 - 2K - c_0H) + 2B\nabla^2 H \quad (6)$$

$$(\boldsymbol{\tau}_2 \cdot \mathbf{n} - \boldsymbol{\tau}_1 \cdot \mathbf{n}) \cdot \mathbf{t} = \nabla_s \gamma \quad (7)$$

(iv) Finally, the formulation is completed by introducing the local area constraint condition $\partial(dA)/\partial t = 0$ [3] in order to find an unknown tension/compression force γ due to the surface force jump given by Eqs. (6) and (7).

Dimensionless parameters in Eqs. (1, 3, 5) are the electric force and electric stress parameters α and ω , respectively, both scaled by the viscous force $V_0\mu/R$, and the characteristic diffusion length κR of the electric double layer based on the Debye length κ^{-1} :

$$\alpha = \frac{\varepsilon \varepsilon_0 \kappa^2 R \zeta^2}{\mu V_0}, \quad \omega = \frac{\varepsilon \varepsilon_0 \zeta^2}{\mu V_0 R}, \quad \kappa = \sqrt{\frac{e^2}{\varepsilon \varepsilon_0 k T} \sum_i (z_i^2 n_i^\infty)} \quad (8)$$

where ε is the relative electric permittivity, ε_0 is the permittivity of the vacuum, and the summation term inside the

expression for Debye length κ represents the ionic strength of the electrolyte solution with z_i and n_i^∞ being, respectively, the valence number and the bulk concentration for each ionic species i . The system of governing equations (1-7) is complemented by the boundary conditions:

$$\mathbf{u}(\mathbf{x}) = 1 \hat{\mathbf{e}}_x, \quad \mathbf{x} \in \partial\Omega_t; \quad \mathbf{u}(\mathbf{x}) = \mathbf{u}_m(\mathbf{x}), \quad \mathbf{x} \in \partial\Omega_m; \quad \mathbf{u}(\mathbf{x}) = 0, \quad \mathbf{x} \rightarrow \infty;$$

$$\phi_1(\mathbf{x}) = \phi_2(\mathbf{x}) = \phi_m, \quad \mathbf{x} \in \partial\Omega_m \text{ toward } \Omega_1 \text{ and } \Omega_2;$$

$$\phi(\mathbf{x}) = 0, \quad \mathbf{x} \rightarrow \infty; \quad \phi_1(\mathbf{x}) = \phi_t(\mathbf{x}), \quad \mathbf{x} \in \partial\Omega_t;$$

$$\varepsilon_r \nabla \phi_t(\mathbf{x}) \cdot \mathbf{n}(\mathbf{x}) = \nabla \phi_1(\mathbf{x}) \cdot \mathbf{n}(\mathbf{x}), \quad \mathbf{x} \in \partial\Omega_t \quad (9)$$

where the relative dielectric constant is defined by $\varepsilon_r = \varepsilon_t / \varepsilon_1$. Several assumptions are made in the boundary conditions to simplify problem: (i) the AFM tip approach speed remains constant during imaging process, (ii) the membrane electric potential is small, $|\phi| \ll \zeta$, so that the Poisson-Boltzmann equation can be linearized, (iii) the polar groups of the lipid molecules keep the electric potential uniform across the membrane, (iv) the AFM tip has zero surface charge density.

Boundary Integral Formulation

The model equations are intimately coupled and solved by the boundary integral method. According to Ladyzhenskaya [9], the integral form of the dimensionless, nonhomogeneous Stokes equation combines the contributions from *Stokeslet*, *Stresslet*, and nonhomogeneous source terms and is given by:

$$\begin{aligned} \lambda u_j(\mathbf{x}_0) = & - \int_{\Omega} S_i(\mathbf{x}) G_{ij}(\mathbf{x}, \mathbf{x}_0) dV(\mathbf{x}) \\ & - \int_{\partial\Omega} \tau_{ik}(\mathbf{x}) n_k(\mathbf{x}) G_{ij}(\mathbf{x}, \mathbf{x}_0) dA(\mathbf{x}) \\ & + \int_{\partial\Omega}^{p.v., \mathbf{x}_0 \in \partial\Omega} u_i(\mathbf{x}) T_{ijk}(\mathbf{x}, \mathbf{x}_0) n_k(\mathbf{x}) dA(\mathbf{x}) \end{aligned} \quad (10)$$

where $\lambda=0$ for $\mathbf{x}_0 \notin \Omega$, $\lambda=8\pi$ for $\mathbf{x}_0 \in \Omega - \partial\Omega$, and $\lambda=4\pi$ for $\mathbf{x}_0 \in \partial\Omega$. Also, the unit surface normal vector n_j points into the fluid domain, S_i represents the vector source term due to Lorentz electric force in Eq. (3), u_i and τ_{ik} represent the velocity and electrohydrodynamic stress fields. Note that when the source point is located at the boundary, $\mathbf{x}_0 \in \partial\Omega$, the double layer Stresslet contribution has to be interpreted in the sense of Cauchy principal value because of the stronger singularity in the integral kernel T_{ijk} . The fundamental solution (*Stokeslet*) and its corresponding stress field (*Stresslet*) are given by [10],

$$G_{ij}(\mathbf{x}, \mathbf{x}_0) = \frac{\delta_{ij}}{r} + \frac{r_i r_j}{r^3}, \quad T_{ijk}(\mathbf{x}, \mathbf{x}_0) = -6 \frac{r_i r_j r_k}{r^5} \quad (11)$$

respectively, where δ_{ij} is the Kronecker delta function, $\mathbf{r} = \mathbf{x} - \mathbf{x}_0$ is the position vector between the field and source points, and $r = |\mathbf{x} - \mathbf{x}_0|$ is the distance between them. Further, the domain integral of the source term $S_i = -\alpha\phi \nabla \phi$ can be

transformed into the surface integral by incorporating the divergence free property of the *Stokeslet*, $\nabla \cdot G_{ij} = 0$, i.e.,

$$\int_{\Omega} \phi \frac{\partial \phi}{\partial x_i} G_{ij} dV = \frac{1}{2} \int_{\Omega} \nabla \cdot (\phi^2 G_{ij}) dV \quad (12)$$

Thus, the boundary integral formulation of Eq. (3) becomes

$$\begin{aligned} \lambda u_j = & - \frac{\alpha}{2} \int_{\partial\Omega} \phi^2 G_{ij} n_i dA \\ & - \int_{\partial\Omega} \tau_{ik} n_k G_{ij} dA + \int_{\partial\Omega} u_i T_{ijk} n_k dA \end{aligned} \quad (13)$$

Eq. (13) is valid for the fluids on both sides of the biomembrane, and the domains can be effectively combined leading to the following unified domain formulation [3]:

$$\begin{aligned} \lambda u_j = & - \int_{\partial\Omega_m} \Delta f_i G_{ij} dA \\ & + \int_{\partial\Omega_t} \left(f_i + \frac{\alpha}{2} \phi_t^2 n_i \right) G_{ij} dA - \int_{\partial\Omega_t}^{p.v., \mathbf{x}_0 \in \partial\Omega_t} u_i T_{ijk} n_k dA \end{aligned} \quad (14)$$

where $\lambda=8\pi$ for $\mathbf{x}_0 \in \Omega_1 + \Omega_2 + \partial\Omega_m$, and $\lambda=4\pi$ for $\mathbf{x}_0 \in \partial\Omega_t$. Note that the traction term is replaced by the surface force $f_i = \tau_{ik} n_k$ for convenience, and the surface force jump condition $\Delta f_i = f_i^{(2)} - f_i^{(1)}$ in the kernel function can be interpreted as the source density acting on the fluid from the cell membrane surface. Clearly, the solution of linearized Poisson-Boltzmann and Laplace equations, Eqs. (1) and (2), can also be expressed in terms of integral equations:

$$\lambda_1 \phi_1 = \int_{\partial\Omega} \left(G_{PB} \frac{\partial \phi_1}{\partial n} - \phi_1 \frac{\partial G_{PB}}{\partial n} \right) dA, \quad (15)$$

$$\lambda_t \phi_t = \int_{\partial\Omega} \left(G_L \frac{\partial \phi_t}{\partial n} - \phi_t \frac{\partial G_L}{\partial n} \right) dA \quad (16)$$

respectively, where $\lambda_1=0.5$ for $\mathbf{x}_0 \in \partial\Omega_t + \partial\Omega_m$, $\lambda_1=1.0$ for $\mathbf{x}_0 \in \Omega_1$, $\lambda_t=0.5$ for $\mathbf{x}_0 \in \partial\Omega_t$, and $\lambda_t=1.0$ for $\mathbf{x}_0 \in \Omega_t$. Note that the coefficient value 0.5 is for the smooth boundary. And the fundamental solutions are given by

$$G_{PB} = e^{-(\kappa r)} / 4\pi r, \quad G_L = 1 / 4\pi r \quad (17)$$

As shown in Fig. (1), the AFM tip and cell membrane are axisymmetric, so the complexity of the integral formulations can be further reduced by using the cylindrical coordinate system and expressing the fundamental solutions in terms of the Green's functions of the ring source type. Finally, the membrane constraint equation can be expressed in terms of the arc-length with the local surface tangent $\hat{\mathbf{t}}(\mathbf{x} \in \partial\Omega_m)$ [3]:

$$\sigma \left(\frac{\partial u_x}{\partial s} \hat{\mathbf{t}}_x + \frac{\partial u_\sigma}{\partial s} \hat{\mathbf{t}}_\sigma \right) + u_\sigma = 0, \quad \mathbf{x}_0 \in \partial\Omega_m \quad (18)$$

In the final form, the complex three-dimensional system of integral equations for the coupled electric field/fluid flow/membrane deformation problem, described by Eqs. (14-16, 18) and boundary conditions Eqs. (6,7,9), is reduced to one-

dimensional form using axisymmetric integral representation and is solved numerically using the boundary element method with discretization along the surface of the AFM tip and the cell membrane [3]. Due to the limited space, the details of all transformations are not shown, but reported elsewhere [3,11].

RESULTS AND DISCUSSION

Hydrodynamic Interactions

We consider three basic interaction processes in respect to direction of the tip movement to characterize the fundamental modes of tip-membrane interactions: first, the AFM tip is approaching an initially horizontal membrane with a constant velocity in positive x direction (forward); second, the tip returns to its initial position moving in negative x direction (reverse); and third, the tip stops at its upper state and the membrane is allowed to freely relax and slowly return to its undeformed horizontal shape (relaxation). It should be noted that the driving mechanisms of the membrane deformation are different than those responsible for the free liquid-liquid interface evolution because of the additional effects arising from the surface bending energy and the local tension or compression force induced by the constant area constraint reflecting the assumption of local membrane incompressibility. The results of presented simulations are based on the geometry of the computational domain defined by the following dimensionless quantities: the AFM tip has total height $10R$ (where R is the tip radius), the tip opening angle is $\pi/3$, and the initial tip-sample separation is $10R$. The dimensionless time step is set to 0.1 and is increased to 1.0 in the final stage of the slow membrane relaxation. A test case with the spontaneous membrane curvature $c_0 = -2.0$ is investigated and the dimensionless bending rigidity $B = 0.1, 1.0, 5.0,$ and 20.0 are used for the simulation of the force-distance curves.

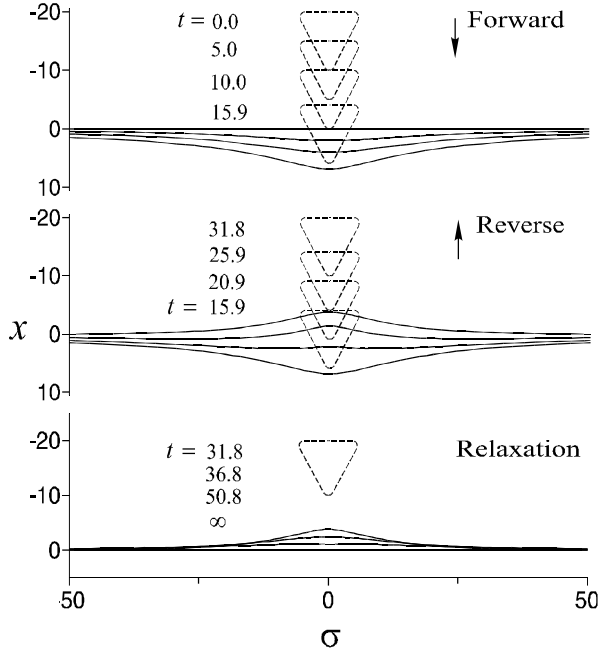


Fig. 2. A full cycle evolution of the fluid membrane with bending rigidity $B = 1.0$ and spontaneous curvature $c_0 = -2.0$ induced by the AFM tip with an opening angle $\alpha = 60^\circ$.

Figure 2 shows the membrane evolution during forward, reverse, and relaxation modes of AFM imaging. As a result of viscous flow induced by an AFM motion in fluid outside the cell, the membrane is pushed forward (bends down) by the hydrodynamic piston force, and the fluid within the cell is in turn moved by the membrane with the highest local velocity around the center location. This coupled behavior of two fluids above and below the membrane is consistent with the continuous velocity distribution and the viscous stress jump condition across the infinitesimally thin cell membrane. The curvature-dependent bending energy continuously changes with the membrane bending, thereby providing a local resistance to any deformation away from the planar, equilibrium state of the membrane with the minimum energy. This resistance causes different transient evolution behavior during forward and reverse modes of AFM operation. In the forward (push) motion mode, an increase in the bending energy induces upward motion of the fluid above the membrane (negative local migration velocities of the fluid 1) against the hydrodynamic (forward directed) forces. On the other hand, in the reverse (pull) mode of operation, a decrease in the bending energy assists initially the membrane to withdraw from its highly deformed bend-down state. However, once the membrane returns to and passes its equilibrium position going upward, the bending energy again starts increasing and begins to resist any further deformation of the membrane until the membrane reaches its maximum negative deformation when the AFM tip stops in its upper position. In the final relaxation stage, the migration of the membrane is slow and solely depends on its bending energy and the fluid viscosity. The flow field evolution shows that the viscous hydrodynamic forces affect the membrane state even in the far field along the radial direction, which is a typical dragging behavior of the Stokes flow. If the simulations are continued for sufficiently long time, the membrane eventually returns to its original equilibrium planar shape and the fluid velocity, the hydrodynamics forces, and the membrane surface forces vanish everywhere.

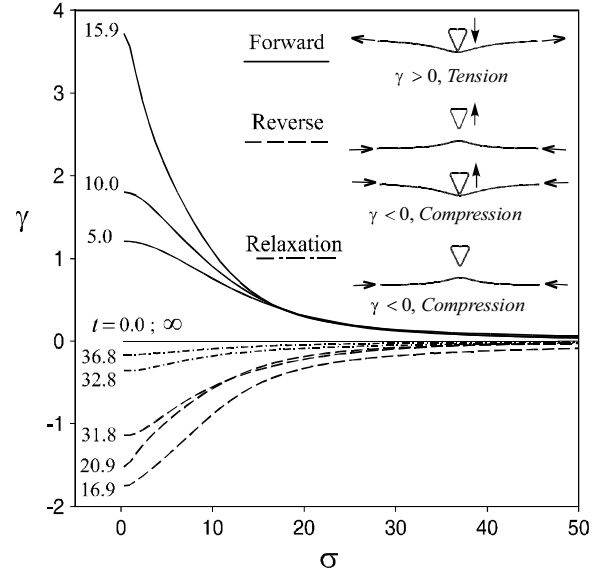


Fig. 3. Isotropic local tension/compression force of deforming membrane with bending rigidity $B = 1.0$ and spontaneous curvature $c_0 = -2.0$ probed by the AFM tip with an opening angle $\alpha = 60^\circ$.

Figure 3 depicts the local isotropic tension ($\gamma > 0$) or compression ($\gamma < 0$) forces in the membrane with respect to the radial position during forward, reverse, and relaxation modes of operation. When the AFM tip is moving forward, the membrane is pushed down by the fluid flow and the tension force is induced to drag the membrane into the center area to satisfy the surface area constraint imposed by the membrane incompressibility. In the reverse motion, compression is observed as the membrane is pulled back and forced to adopt a new shape with smaller area. Even when the membrane recedes over its neutral equilibrium position in the reverse motion (Fig. 2), the surface force is still in the compression mode because the strong hydrodynamic forces overcome the force induced by the slow membrane self-relaxation, thereby maintaining the compression state of the membrane on a shorter time scale.

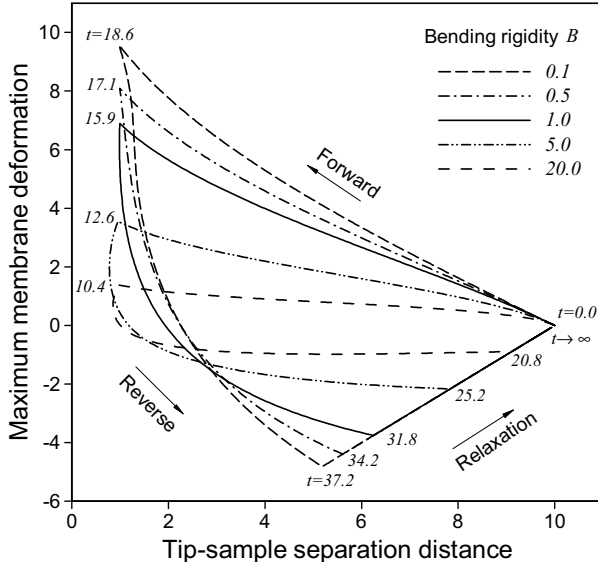


Fig. 4. Effect of the bending rigidity on the hysteresis curve of the membrane deformation vs. tip-sample separation distance for the membrane with spontaneous curvature $c_0 = -2.0$ and the AFM tip opening angle $\alpha = 60^\circ$.

Figure 4 shows the instantaneous maximum deformation of the membrane (at the center) as a function of the instantaneous tip-membrane separation distance in a full cycle simulation. Clearly, this plot is analogous to the typical sampling force-distance curves obtained experimentally during actual AFM imaging of biological cells. The larger bending rigidity translates into stronger membrane resistance to deformation as demonstrated by the smaller variation range for the trace curve along the y-axis. At the same time, when bending rigidity is sufficiently large, the membrane can move faster than an AFM tip initially during the reverse operation mode, which is caused by the strong bending force acting on the membrane. This fact is manifested on Fig. 4 by a decrease of the tip-membrane separation distance below 1.0 at the time moment just past 12.6, for the case of $B = 5.0$. The lagging response is also observed when the minimum tip-membrane separation distance (equal to 1.0) is maintained at time $t = 18.6, 15.9,$ and 12.6 for the cases with bending rigidity $B = 0.1, 1.0,$ and 5.0 , respectively. In the AFM imaging experiments, such an irreversible ‘‘hysteresis’’ behavior in respect to the forward and reverse motion of an

AFM tip is frequently observed for soft samples, and our simulations provide the first theoretical evidence that this behavior is due to coupling of hydrodynamic and elastic membrane effects.

AFM Feedback Force

The total force acting on the AFM tip is due to: (i) the electrohydrodynamic stress owing to the electrically (Lorentz force) driven fluid motion, and (ii) the Maxwell stress generated by the electric field in the vicinity of the AFM tip induced by the charged biomembrane. The first part is obtained by direct integration of the integral solution f_i of Eq. (14) along the surface boundary of the AFM tip,

$$\mathbf{F}_{tip}^{eh} = 2\pi \int_{\partial\Omega_t} \sigma f_i dl \quad (19)$$

and the second part, contributed by Maxwell stress, is obtained by surface integration of the solution ϕ_i of Eq. (15),

$$\mathbf{F}_{tip}^M = 2\pi\omega \int_{\partial\Omega_t} \sigma \frac{\partial\phi}{\partial x} \frac{\partial\phi}{\partial n} - \frac{\sigma}{2} \left[\left(\frac{\partial\phi}{\partial x} \right)^2 + \left(\frac{\partial\phi}{\partial\sigma} \right)^2 \right] n_x dl \quad (20)$$

The Maxwell stress contribution to the force acting at the AFM tip, given by Eq. (20), has been studied before, see for example [12]. Here we only demonstrate the electrohydrodynamic effects by considering three basic interaction processes in respect to direction of the tip movement to characterize the fundamental modes of tip-membrane interactions: first, the AFM tip approaches an initially horizontal membrane with a constant velocity in positive x direction (*forward*); second, the tip returns to its initial position moving in negative x direction (*reverse*); and third, the tip stops at its upper state and the membrane is allowed to freely relax and slowly return to its undeformed horizontal state (*relaxation*). Three typical cases A to C with increasing ionic strength of the electrolyte solution are examined and compared to the purely hydrodynamic case D. The results are shown in terms of the AFM force-distance curve for the tip with 60° opening angle, constant tip approach speed, the membrane bending rigidity $B = 1.0$, and the relative dielectric constant $\epsilon_r = 0.075$. AFM tip velocity, electrolyte viscosity and electrical permittivity are given by the following set ($V_0 = 10^{-5} m/s, \mu = 1.5 \times 10^{-3} kg/m/s, \epsilon_1 = 80$). The test conditions are listed in Table 1.

Table 1: Simulation conditions

A	B	C	D
$R = 50 nm$	$15 nm$	$5 nm$	$50 nm$
$\kappa^{-1} = 96 nm$	$30.4 nm$	$9.6 nm$	∞
$n_c^\infty = 10^{-5} M$	$10^{-4} M$	$10^{-3} M$	0
$\kappa R = 0.52$	0.493	0.52	0
$\alpha = 160$	479	1601	0
$\omega = 590$	1968	5903	0
$\phi_m = \pm 0.25$	± 0.5	± 0.5	0

where n_c^∞ is a representative ionic strength with 1:1 electrolyte concentration.

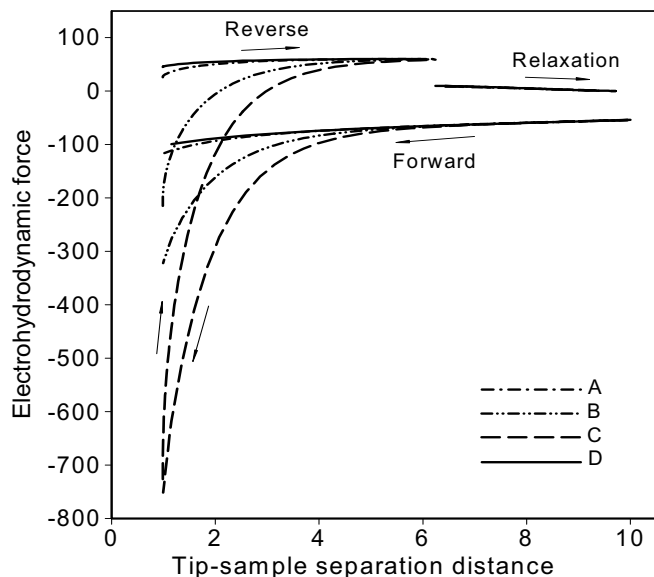


Fig. 5: Electrohydrodynamic force (scaled by $V_0 \mu R$) vs. tip-membrane separation distance (scaled by R) in a full probing cycle for varying ionic strength of the electrolyte.

Figure 5 compares the force vs. tip-to-membrane separation curves for the purely hydrodynamic system [3] and when Lorentz force contribution is taken into account. The results show that the homogeneous Stokes system (i.e., case D with no Lorentz force) can be a good approximation for the system A owing to its low ionic strength. At higher ionic strength (system B) the Lorentz force contribution increases as the AFM tip approaches the electric double layer of the membrane, and it becomes significant when the AFM tip is penetrating into the double layer (i.e., smaller tip-to-membrane distances). For the system C the strong ionic effect exists for an entire probing cycle (i.e., in the near and far fields) because of the very large ionic strength of the electrolyte solution. In the cases B and C, even in the reverse motion of the AFM tip, the repulsive electric force overcomes an attractive hydrodynamic force and dominates the system dynamics. Also, as the ionic strength increases, the strong screening effect confines the electric double layer into a small region near the membrane and the system can be practically separated into two distinctly different domains. Outside of the double layer, the AFM tip is controlled by the purely hydrodynamic attractive forces well described by the homogeneous Stokes system; whereas when the AFM tip penetrates into the thin double layer, the feedback force is dominated by the strongly repulsive osmotic pressure forces and the viscous fluid forces can be neglected. Analysis of governing equations and numerical tests show that the feedback force acting at the AFM tip is mainly controlled by (i) the two correlated dimensionless parameters, α and κR , (ii) the separation distance between an AFM tip and membrane relative to the double layer thickness, and (iii) the membrane surface charge and the material dielectric constants. When Maxwell stress is accounted for, one more dimensionless parameter ω needs to be considered to assess contribution of the Maxwell stress relative for Lorentz and hydrodynamic viscous forces.

CONCLUSIONS

We have investigated fluid mechanics of the AFM imaging of biological membranes in physiological environment to describe the mechanisms of the elastic deformation of the soft sample induced by the AFM tip probing action from the fluid mechanics perspective. In the full probing cycle, a number of interesting and sometimes counterintuitive phenomena was observed such as: (a) dominance of the compression force in the membrane in the reverse (pull-back) mode of operation even after the membrane passes its equilibrium state; (b) a local instantaneous decrease in separation between the AFM tip and the membrane in the beginning of the reverse mode operation when bending rigidity of the membrane is sufficiently large; and (c) the “lagging” behavior (i.e., when the AFM tip-to-membrane separation distance does not change with a decrease in the membrane deformation in the reverse mode of operation) lasts longer in the case of softer membrane with smaller bending rigidity. Relative contributions of the electric Lorentz and hydrodynamic viscous forces to the feedback force acting on the dielectric AFM tip during tapping mode imaging of biomembrane in the electrolyte solution have been quantified. Finally, perhaps the most profound result of this study is that the “hysteresis” observed in the probing experiments using AFM for imaging soft biological samples is due to strong coupling of hydrodynamic effects (fluid motion) and elastic deformation of the membrane. The proposed theoretical methodology provides new insight and quantitative information that cannot be directly measured during the AFM experiment, but essential for interpretation of the imaging data.

ACKNOWLEDGMENTS

National Science Foundation provided financial support for this work through Biocomplexity in Environment Initiative.

REFERENCES

- [1] Lal, R. and John, S.A. (1994), *Am.J. Physiol.* **266**, C1-C21.
- [2] Kamm, R.D. (2002), *Annu. Rev. Fluid Mech.* **34**, 211-232.
- [3] Fan, T.H. and Fedorov, A.G. (2002), *Langmuir* (in press).
- [4] Israelachvili, J.N. (1998), *Intermolecular and surface forces*, Academic Press, San Diego.
- [5] Melcher, J.R. and Taylor, G.I. (1969), *Annu. Rev. Fluid Mech.* **1**, 111-146.
- [6] Landau, L.D. & Lifshitz, E.M. (1959), *Fluid Mechanics*, Pergamon Press, London.
- [7] Helfrich, W. (1973) *Z. Naturforsch. Teil C* **28**, 693.
- [8] Ou-Yang Zhong-can (2001), *Thin Solid Films* **393**, 19-23.
- [9] Ladyzhenskaya, O.A. (1969), *The mathematical theory of viscous incompressible flow*, Gordon & Breach, New York.
- [10] Pozrikidis, C. (1992), *Boundary integral and singularity methods for linearized viscous flow*, Cambridge University Press, Cambridge.
- [11] Fan, T.H. and Fedorov, A.G. (2003), *NANOTECH'03*, San Francisco, California, February 23-27, 2003.
- [12] Butt, H.-J. (1992), *Nanotechnology* **3**, 60-68.